Volume 8 · No. 18 – September 24 2012

NANO MICRO

small

www.small-journal.com

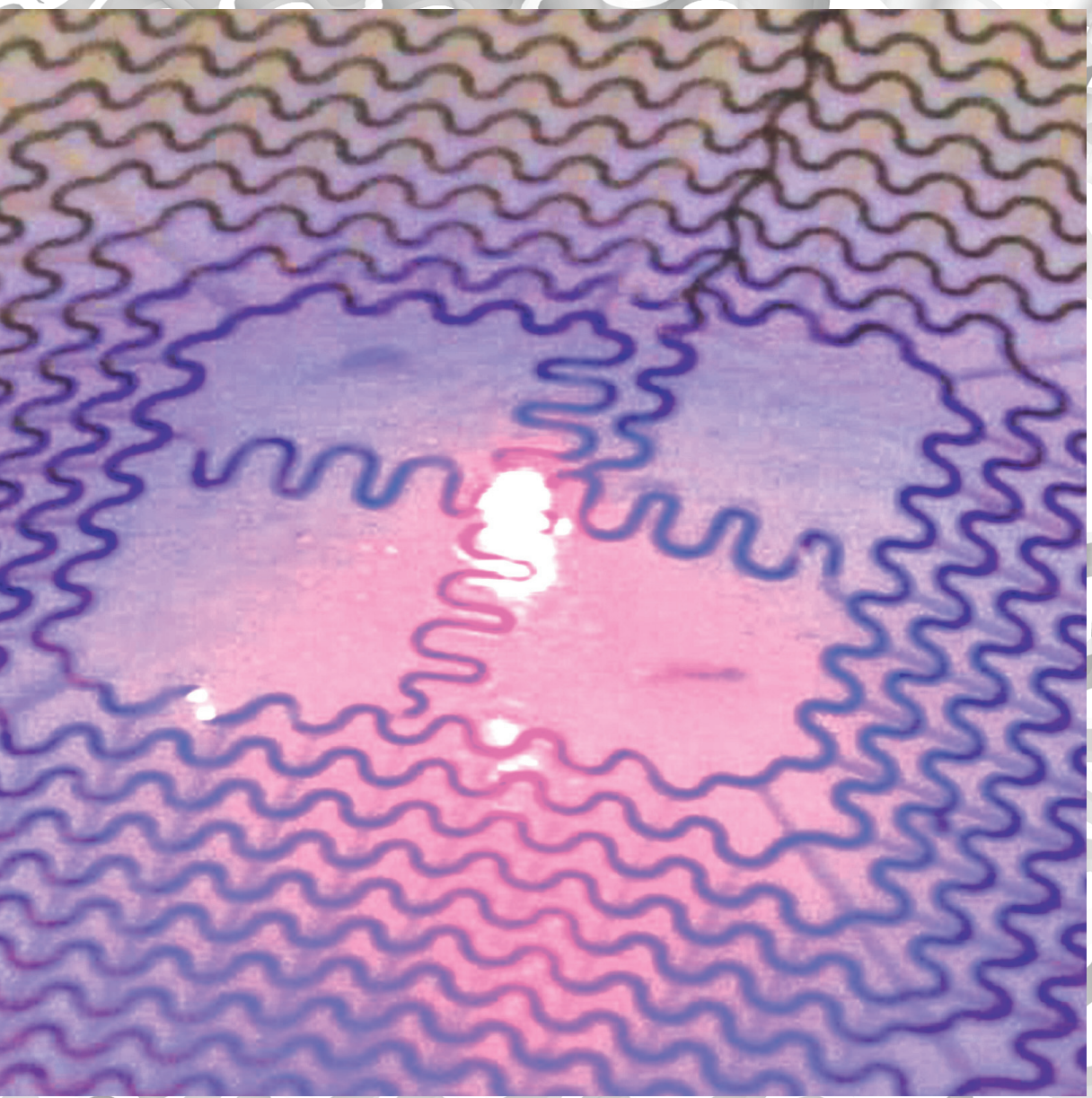

18/2012

WILEY-VCH

Materials and Designs for Wirelessly Powered Implantable Light-Emitting Systems
F. G. Omenetto, J. A. Rogers et al.

Materials and Designs for Wirelessly Powered Implantable Light-Emitting Systems

Rak-Hwan Kim, Hu Tao, Tae-il Kim, Yihui Zhang, Stanley Kim, Bruce Panilaitis, Miaomiao Yang, Dae-Hyeong Kim, Yei Hwan Jung, Bong Hoon Kim, Yuhang Li, Yonggang Huang, Fiorenzo G. Omenetto, and John A. Rogers**

Recent developments in flexible/strechable electronics[1–3] and optoelectronics[4–6] demonstrate that high-performance semiconductor device functionality can be achieved in forms that enable intimate, conformal contacts to static or time-dynamic curvilinear surfaces,[7,8] with promising applications in advanced biomedical devices and other areas that cannot be addressed with conventional technologies. For many clinical uses of such devices, the ability to provide continuous or periodic powering in a wireless mode is highly desirable.[9–11] Here, we present a route to flexible and stretchable systems of microscale inorganic light-emitting diodes (μ-ILEDs) with wireless powering schemes, for implantable devices that could be used to accelerate wound healing,[12–14] activate photosensitive drugs,[15–17] or to perform imaging and spectroscopic characterization of internal tissues.[18,19] We emphasize in the following aspects of materials, mechanics, and thermal physics that enable systems of this type.

R.-H. Kim,[+] Dr. T.-i. Kim,[+] S. Kim, Y. H. Jung, Dr. B. H. Kim, Prof. J. A. Rogers
Department of Materials Science and Engineering
Frederick Seitz Materials Research Laboratory
University of Illinois at Urbana-Champaign
Urbana, IL 61801, USA
E-mail: jrogers@illinois.edu

Dr. H. Tao,[+] Dr. B. Panilaitis, M. Yang, Prof. F. G. Omenetto
Department of Biomedical Engineering
Tufts University
Medford, MA 02155, USA
E-mail: fiorenzo.omenetto@tufts.edu

Dr. Y. Zhang, Dr. Y. Li, Prof. Y. Huang
Departments of Civil and Environmental Engineering, and Mechanical Engineering
Northwestern University
Evanston, IL 60208, USA

Prof. D.-H. Kim
School of Chemical and Biological Engineering
Institute of Chemical Processes
Seoul National University
Seoul 151-741, Republic of Korea

Dr. B. H. Kim
Department of Materials Science and Engineering
Korea Advanced Institute of Science and Technology (KAIST)
Daejeon 305-701, Republic of Korea

Dr. Y. Li
School of Astronautics
Harbin Institute of Technology
Harbin 150001, China

Prof. J. A. Rogers
Departments of Chemistry
Mechanical Science and Engineering
Electrical and Computer Engineering
Beckman Institute for Advanced Science and Technology
University of Illinois at Urbana-Champaign
Urbana, IL 61801, USA

[+] R.-H.K., H.T, and T.-i.K. contributed equally to this work.

DOI: 10.1002/smll.201200943

Figure 1 illustrates the designs and main fabrication steps. The first part involves preparation of μ-ILEDs in formats that are compatible with techniques for integration by transfer printing.[20,21] For work described here, thin (~6.54 μm) epitaxial semiconductor layers (p-GaN/ multiple quantum wells (InGaN/ GaN)/ n-GaN/ buffer layer/ GaN) grown on (0001)-oriented sapphire substrates serve as active materials. The layer configuration appears in Figure S1 (Supporting Information, SI). As shown in the inset optical micrograph, the fabrication, whose details appear elsewhere,[21] yields arrays of fully formed InGaN μ-ILEDs (100 μm × 100 μm) with n-type (Cr: 15 nm/ Au: 300 nm) and p-type ohmic contacts (Ni: 15 nm/ Au: 15 nm) on sapphire (Figure 1a). Laser induced lift-off to a silicon wafer (Figure 1b) followed by transfer onto a structured substrate (details appear in Figure S2, SI) of poly(dimethylsiloxane) (PDMS) yields print-ready devices. Selective transfer printing delivers μ-ILEDs in desired layouts to a temporary carrier substrate (glass) coated with a bilayer of epoxy (SU8-2; Microchem.; 1 μm thick; ε_r (dielectric constant)= 3.2 at 10 MHz; loss tangent = 0.04 at 10 MHz)[22]/ poly(methylmethacrylate) (PMMA A2; Microchem.; 100 nm thick). The second part of the processing uses adapted versions of procedures described elsewhere,[23] to yield patterned interlayer dielectric polymers (epoxy; 6.8 μm), interconnects and inductive coils (Cr (30 nm)/ Au (1000 nm) and top electrodes (Cr (30 nm)/ Au (500 nm)), with a final, encapsulating passivation layer of epoxy (1.5 μm). Here, the rectangular spiral inductor coil and the straight interconnect lines terminate at the p- and n-type ohmic contacts, respectively, with a thin (~1 μm) layer of epoxy to separate these lines at their crossing points. A schematic illustration of the resulting system is provided in Figure 1c. Detailed geometries and dimensions of the metal interconnects appear in the optical micrograph (top frame) and the schematic illustration (bottom frame) of Figure 1d.

small NANO MICRO

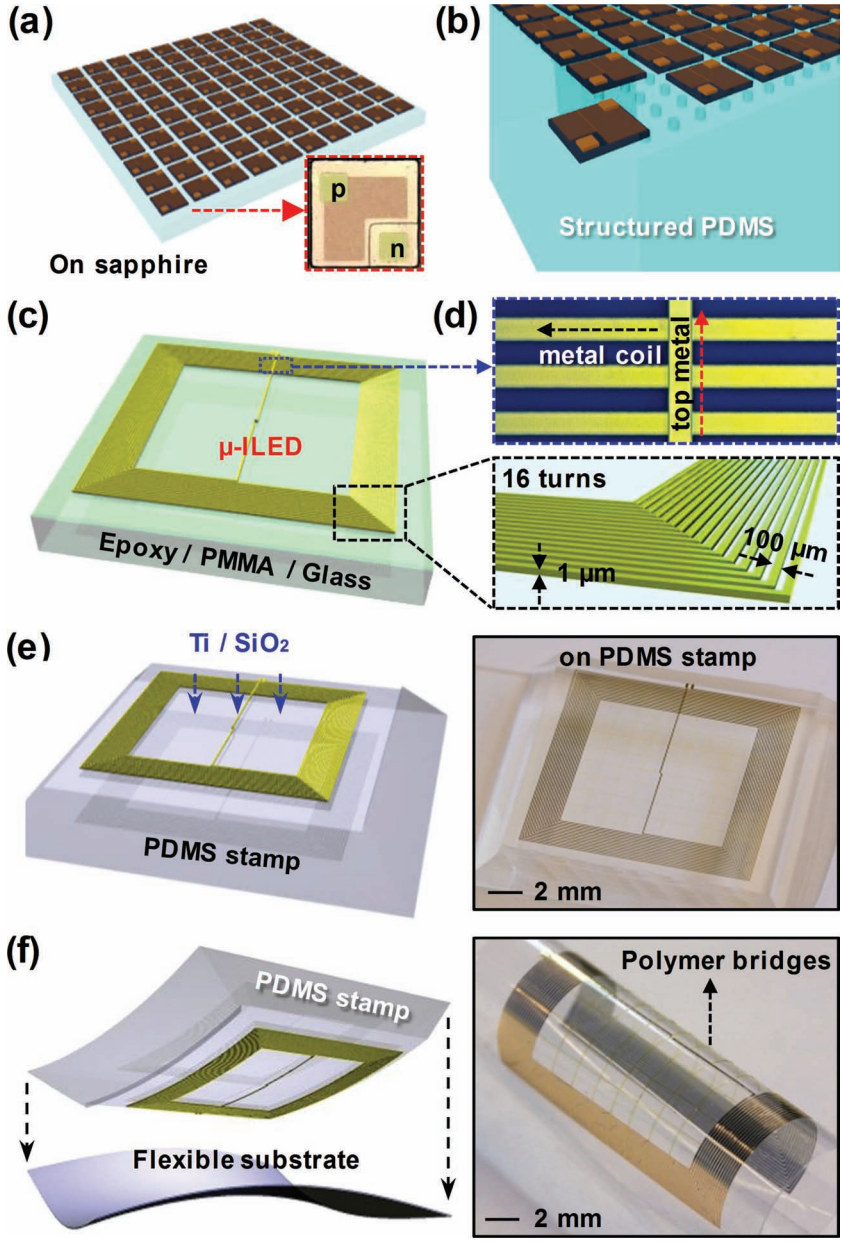

Figure 1. a) Schematic illustration of an array of fully formed, InGaN μ-ILEDs (100 μm × 100 μm, thickness ~6.54 μm) with ohmic contacts on a sapphire substrate. b) Illustration of InGaN μ-ILEDs, after delivery onto a slab of PDMS with a structured surface. c) Illustration of a wireless μ-ILED system on a temporary glass substrate coated with a bi-layer of epoxy/ PMMA. After selective transfer printing of μ-ILEDs, formation of two photopatterned layers of epoxy and two metallization processes define interconnects and wireless coils. d) Optical micrograph (top frame) showing the interconnect scheme, consisting of a planar spiral coil (connected to p-type ohmic contact) and a bridging metal electrode (connected to n-type ohmic contact). A layer of epoxy separates the two metal layers at their crossing points. Detailed dimensions of the planar spiral coil appear in the bottom frame. e) Illustration (left frame) and corresponding optical image (right frame) of a wireless μ-ILED system, retrieved with an elastomeric stamp after removal of the PMMA. Deposition of Ti/ SiO_2 covers the backside of the device, as preparation for bonding on a target substrate. f) Schematic illustration of the process for transferring onto a flexible sheet (left frame) and optical image of a wireless μ-ILED system on a PET substrate (right frame) in its bent state (bending radius = 0.75 cm).

The third and final part of the process involves releasing the device and integrated inductor coil from the carrier substrate, to yield a complete, flexible or stretchable system upon mounting on a suitable substrate. The layouts exploit segmented mesh-type designs connected mechanically by polymer (i.e., epoxy/ PMMA) bridges (Figure S3, SI) and released by dissolving the PMMA layer and transferring to a PDMS slab. Depositing a thin layer of Ti/ SiO_2 (3 nm/ 30 nm), as shown in the schematic illustration and the optical image of Figure 1e, prepares the surface for bonding to a substrate of interest. The optical image of Figure 1f shows a representative flexible wireless μ-ILED system on a thin (50 μm) sheet of PET (polyethylene terephthalate) in its bent state (bending radius = 0.5 cm). A cross-sectional view appears in Figure S4 (SI).

The critical design parameters for the wireless coils include trace width, spacing, thickness, and numbers of turns. Choices of these parameters can be determined by electrical characterization of individual μ-ILEDs and integrated systems. As illustrated in **Figure 2**a, current–voltage (I–V) measurements of a μ-ILED with a rectangular spiral coil show the same turn-on voltage (at $I = 20$ μA) as an otherwise identical μ-ILED without the coil, but with a slightly higher resistance (i.e., lower slope; increase of ~0.9 V to maintain a current of 1 mA) due to the additional line resistance of the coil. Increasing the thickness of the metal (here ~1 μm) minimizes this resistance. Because the systems reported here do not include rectifiers, the transmitted alternating current (AC) power from the primary coil appears directly at the μ-ILED, through the receiving coil. The equivalent electrical circuit diagram for this system is shown in Figure S5a (SI). As a result, the AC response of the μ-ILED in the radio frequency (RF) range is important to consider. Figure 2b summarizes the peak voltages (V_{peak}) required to achieve fixed brightness from a μ-ILED, as a function of operating frequencies. The data show a monotonic increase in the peak voltage with frequency (sine wave, see Figure S5b, SI), to an extent that leads to reverse-bias breakdown in attempts to operate the device at frequencies above ~60 MHz, qualitatively consistent with behaviors in conventional LEDs.[24,25] Based on these considerations, we used coils with resonance frequencies below 50 MHz where many subdermal implants have been reported; dielectric relaxation losses in biological tissues tend to increase dramatically at high frequencies (typically, >1 GHz).[26] The left frame of Figure 2c shows an example during operation via inductive coupling at 40.9 MHz

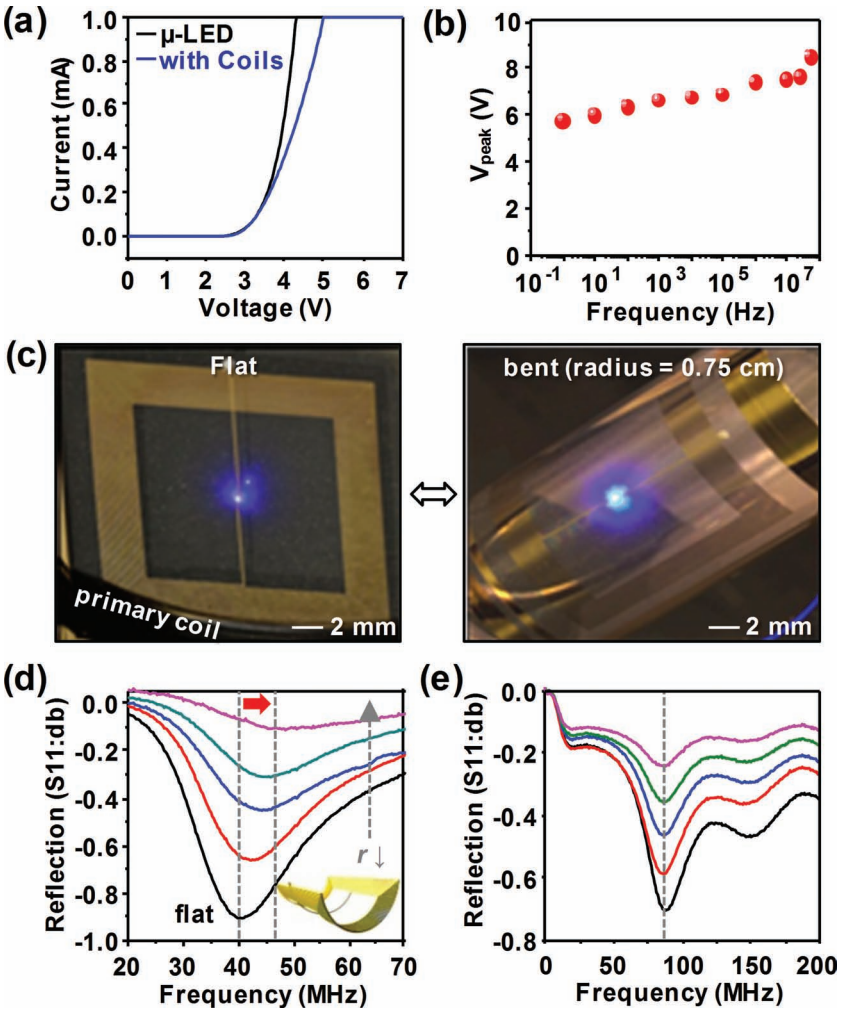

Figure 2. a) The current–voltage (*I–V*) characteristics of an individual μ-ILED with and without integrated spiral inductor coils (The spiral coils have dimensions shown in Figure 1). b) Peak voltages needed to produce currents of 0.1 mA as a function of operating frequency when operated in an alternating current mode. c) Optical images of a wireless μ-ILED system on a PET substrate powered via inductive coupling at an appropriate resonance frequency in its flat (left frame) and bent (right frame) state. d) Measured scattering parameter, S11 as a function of bending radius in a concave shape (sample dimension = 4 cm^2). e) Measured scattering parameter of inductor coils with reduced dimensions, as a function of bending radius in a concave shape (sample dimension = 1 cm^2).

(consistent with separate measurements of an isolated primary coil (1 turn number, diameter = 5 cm, 12 AWG) with an external supply (input power = 22.3 dBm, detailed setup appears in Figure S5c, SI). Flat configurations such as this one offer ideal operating characteristics, but the designs also function in deformed or bent states. The right frame of Figure 2c shows an optical image of a system powered via inductive coupling (operating frequency = 48.5 MHz, input power = 23.4 dBm), while sharply bent (r = 0.75 cm). The observed increase in required input power is consistent with a corresponding change in the scattering parameter, S11, induced by concave bending (inset schematic illustration; this deformation places the device layers in compression), as evaluated on an isolated coil using a network analyzer (HP 8573D, see Figure S6a, SI) and a surface mount assembly (BNC, see Figure S6b, SI). Figure 2d shows the resonant characteristics of the device of Figure 2; the result reveals a systematic increase and decrease in resonance frequency and peak amplitude, respectively, with decreasing bending radius. A bending radius of 1 cm induces a ~21% increase in resonance frequency and ~90% decrease in the peak amplitude (Figure S7a, SI), implying significant reduction in the power transfer efficiency and, as a result, the operating range of the system, even if the primary coil is adjusted to match the shifted resonance frequency of the receiver. These observations can be explained by bending induced decreases in the inductance, which are linearly proportional to the area (or projected area) of a coil enclosed by a current loop, according to electromagnetism theory.[27] The damped resonance characteristics with bending are due, at least in part, to increases in the effective distance between the primary and receiver coils. Such disadvantages can be relaxed by reducing the overall dimensions of the system (also advantageous in implantable devices), to decrease the sensitivity to the curvature, in terms of the projected area, and the effective separation distances, as shown in Figure S8 (SI). In good agreement with such expectations, the sample with smaller dimensions (1 cm^2) shows no noticeable dependence of resonance frequency on concave bending (Figure 2e and Figure S7b, SI). The peak amplitude shows trends similar to those of the larger devices, but with less significant decreases (~65% decrease at a bending radius of 1 cm).

Simple changes in the metal interconnect schemes (i.e., inductor coils) or introduction of stacked geometries represent other possibilities of interest. For example, **Figure 3**a presents optical images of a system with four μ-ILEDs, in flat (inset image of Figure 3a) and bent (Figure 3a, r (radius of curvature)= 3 cm) states, driven with a single spiral inductor coil (number of turns = 16, size = 4 cm^2) at a frequency of 27.5 MHz. The slight non-uniformity in brightness is due to an uneven distribution of current that occurs in this parallel interconnection scheme due to slight variations in device performance (the μ-ILED indicated by the red arrow has relatively low output). Uniform emission characteristics can, nevertheless, by achieved in many cases, as shown in the inset image of **Figure 4**g. The measured scattering parameter, S11 reveals RF characteristics similar to those of the system with a single μ-ILED (Figure 2d) in various bending deformations (concave and convex) as shown in Figure 3b.

Replacing the straight inductor coils with those that have serpentine shapes (Figure 3c) yields systems that can be stretched, i.e., capable not only of bending but of accommodating large strain (>1%) deformations with linear

small NANO MICRO

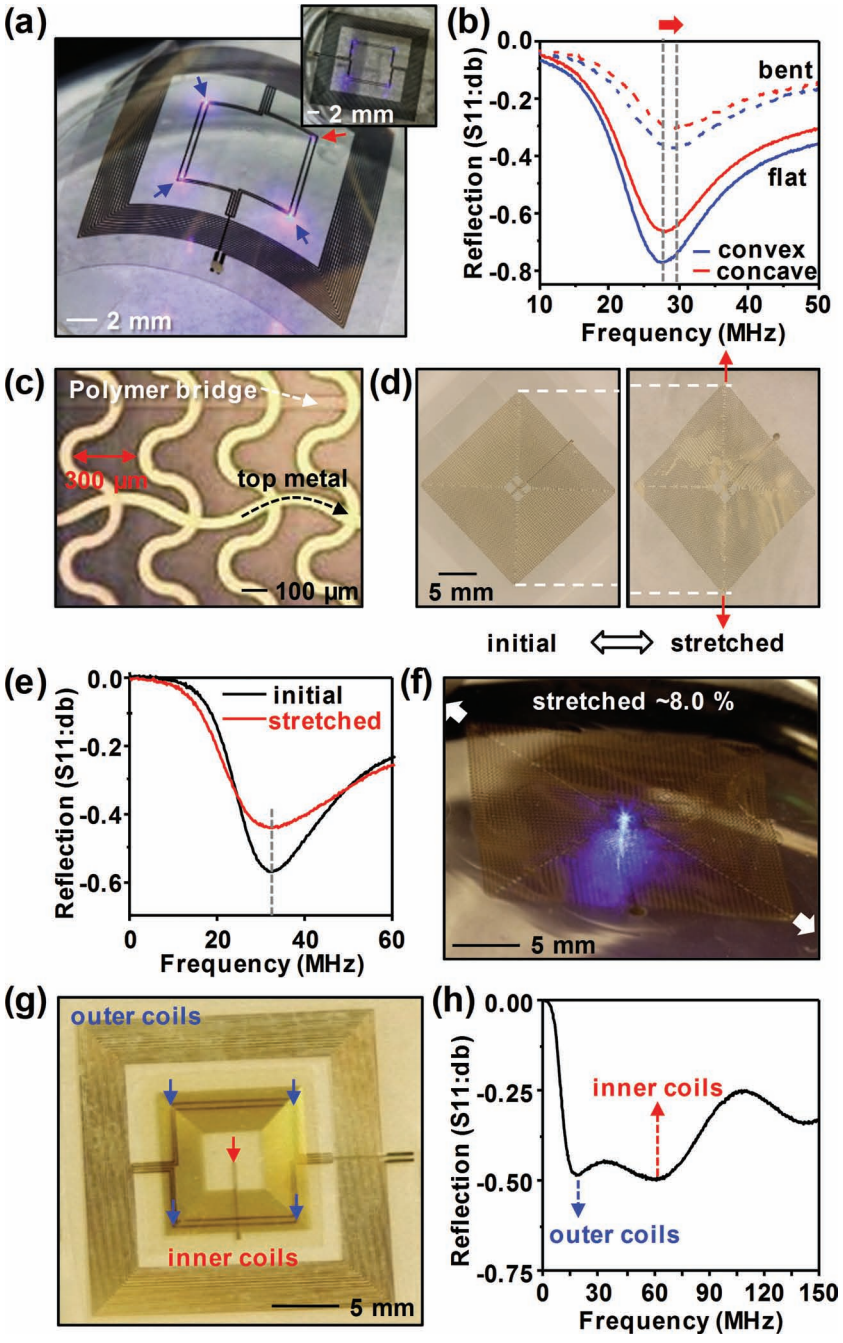

Figure 3. a) Optical image of a wireless system that includes four μ-ILEDs connected in parallel, powered via inductive coupling. b) Measured scattering parameter, S11 in flat (solid line) and bent (dashed line) states (concave: blue, convex: red). c) Optical micrograph showing the interconnect scheme for a stretchable design. Both spiral and cross-over metal lines adopt serpentine shapes, separated by a thin layer of epoxy at their crossing points. d) Optical images of a wireless μ-ILED device in a stretchable format integrated on a thin slab of PDMS in its initial unstretched (left frame) and stretched (right frame; ~8% along the direction indicated by red arrows in the figure) states. e) Measured scattering parameter, S11 in unstretched (color in black) and stretched (color in red) states. f) Optical image of a wireless μ-ILED system when stretched along the diagonal direction (~8%, indicated by arrows). Image was collected while powering the device via inductive coupling. g) Optical image of a stacked wireless μ-ILED device formed by multilayer lamination. The red and blue arrows correspond to μ-ILEDs integrated with the smaller and larger coils, respectively. A wireless μ-ILED system with reduced overall size (~1 cm × 1 cm) printed on top of one with larger size (~2 cm × 2 cm). h) Measured scattering parameter, S11 of the integrated, stacked system.

elastic mechanics. (Such serpentine coils require additional space for the traces. In particular, the line spacings increase from 100 to 300 μm, as indicated by a red arrow in Figure 3c). To compensate for the increase in resonance frequency caused by the increase in spacings, we incorporated additional turns in the serpentine coils (from 16 to 30) and reduced the line widths (from 100 to 75 μm); the result removes any significant change in frequency. RF characteristics of serpentine coils with different numbers of turns are provided in Figure S9 (SI). The completed stretchable device, supported by a thin (~300 μm) sheet of PDMS, appears in Figure 3d in flat (left frame) and stretched (right frame) configurations (enlarged images appear in Figure S10a, SI). The measured scattering parameter (S11 for both cases in Figure 3e) indicates that the peak amplitude in the stretched state slightly decreases, with no noticeable change in resonance frequency. An optical image of a device stretched by ~8% along the diagonal direction, and powered with a primary coil at a frequency of 32.4 MHz, is provided in Figure 3f (~7% compressed state appears in Figure S10b, SI). Fracture occurred beyond ~8%, primarily at crossed edges, as indicated in Figure S10c (SI). This behavior is consistent with finite element analysis (FEA), which shows stress concentrations at the crossed edges (see Figure S11 and SI text for details). FEA also suggests that enhanced stretchability can be obtained by adopting larger metal thicknesses (Figure S12a, SI) or narrower trace widths, using substrates with lower elastic modulus (Figure S12b, SI), and/or increasing the radius of curvature of serpentine coils.

As another possibility, multilayer stacked geometries can offer the ability to operate different μ-ILEDs at different driving frequencies. Separately fabricated systems that have different resonance frequencies can be co-integrated on a single substrate, using an interlayer dielectric and adhesive of PDMS (~50 μm thick). Figure 3g and Figure S13a (SI) show an optical image and a schematic illustration, respectively. A sheet of PET serves as the support for a μ-ILED with a first coil (size = 1 cm^2, metal width = 25 μm, and turn numbers = 60), in a system with the dimensions of the one in Figure 3a integrated on top. The resonance frequency in this stacked

geometry is provided in Figure 3h, showing two weak but noticeable resonances that match the resonances of individual devices before co-integration with slight offsets due to the mutual coupling between the coils (Figure S13b, SI, shows the resonance frequency before co-integration).

Solid-state lighting devices have various possible applications in bio-medicine, ranging from phototherapy (e.g., accelerating wound healing and mitigating infection),[12–14] to photodynamic drug delivery,[15–17] to spectroscopic characterization of arterial blood[28] and cognition,[29] to optogenetics.[30] Together with recent developments in flexible electronics/optoelectronics, the wireless operation capability introduced here enables such devices to be exploited in forms designed for these and other purposes. The small sizes of μ-ILEDs are important because they facilitate passive thermal spreading, and enable integration using planar processing, in water-proof forms. Figure 4a shows thermal images of a wireless μ-ILED and integrated coil, operated via inductive coupling at a resonance frequency of ~30 MHz with different input powers (corresponding optical images appear in Figure S15a, SI). The system uses a thin (50 μm) sheet of PET as a substrate, mounted on a plastic plate (~1.2 mm thick polystyrene, thermal conductivity: 0.156 $W \cdot m^{-1}K^{-1}$) for the measurements. The results show that heat is mostly generated (ambient temperature = 21.9 °C) and localized at the μ-ILED. As the input power increases (from left to right images), the peak temperature of the μ-ILED increases linearly with negligible changes in the temperatures of the interconnect regions (i.e., inductor coils)

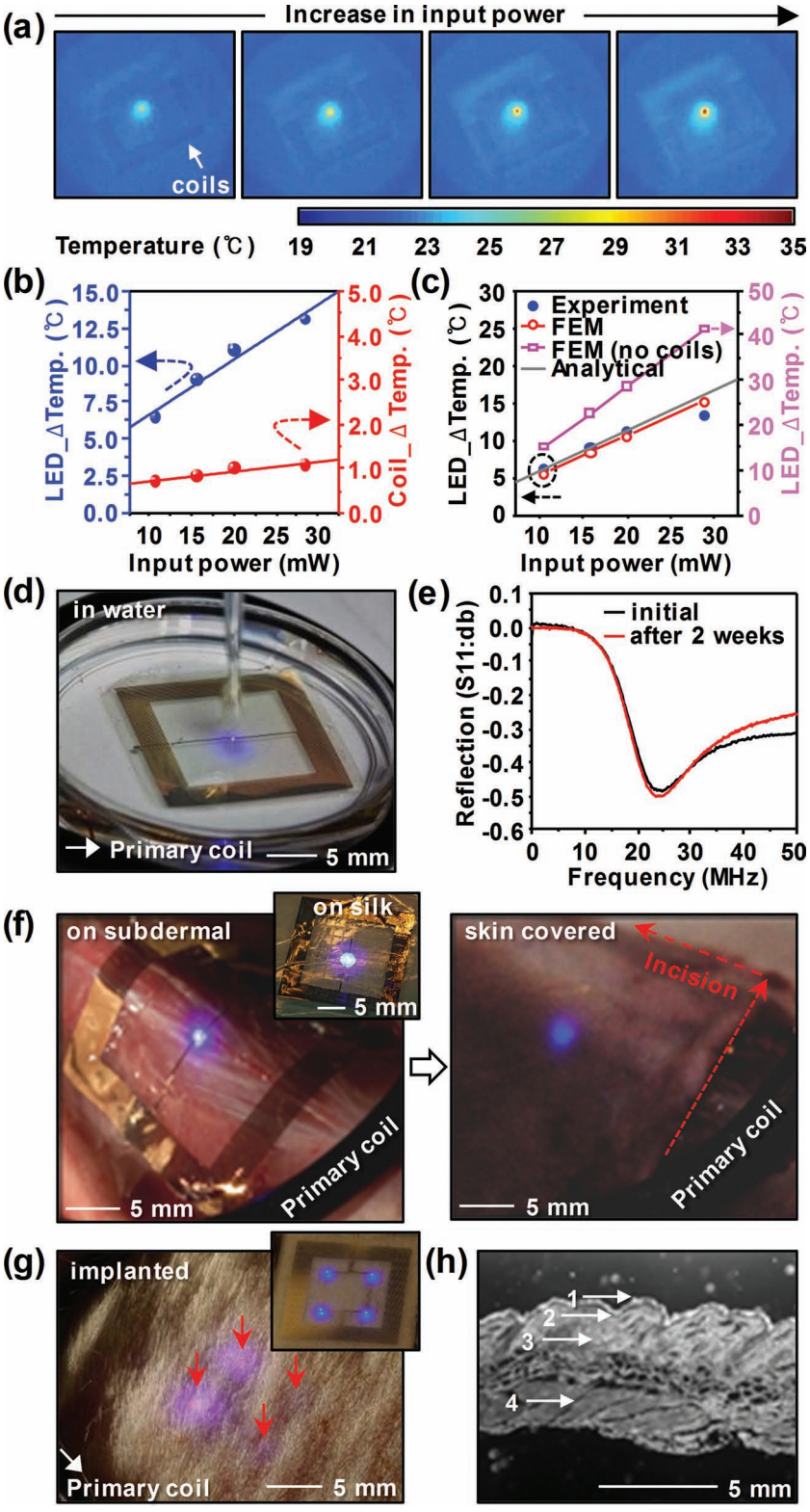

Figure 4. a) Thermal images of a wireless μ-ILED system on a PET substrate at increasing input power (10.73, 15.72, 20.08, and 28.55 mW from left to right frames). b) Graphical representation of the increase in the peak temperature of the μ-ILED and interconnects (i.e., spiral coils). The surrounding temperature was 21.9 °C. c) Temperature increases predicted by analytical models and 3D FEA simulations. d) Optical image of a wireless μ-ILED system on PET, completely immersed in water. The image was collected during inductive operation. e) Measured scattering parameter, S11 before and after immersing the system in a PBS solution for two weeks. f) Wireless μ-ILED system, laminated on the sub-dermal region of a mouse model (left frame). The device was driven by inductive coupling. The inset image provides the initial form of the device, integrated on a silk substrate. The optical image in the right frame corresponds to the state after covering the device with the dermis. The image is collected during operation, via inductive coupling through the skin. The exposure time of camera was set to 10 s for ease of viewing of blue light emission from the μ-ILED. g) Image of an animal model with a wireless μ-ILED device implanted under the skin, and on top of the muscle tissue. The inset shows the device before implantation where four μ-ILEDs are integrated on a PET substrate. h) Histological section of tissue at the implant site, excised after 3 weeks (1, corneum; 2, epidermis; 3, dermis, 4, muscular layer).

as shown in Figure 4b. Analytical models and FEA of heat conduction (see SI text for details) reveal the mechanisms for heat dissipation and provide guidelines to minimize adverse thermal effects. Analytical solutions for surface temperatures agree well with experiments and FEA (Figure 4c and Figure S15b, SI). These models show that the inductor coil plays a critical role in the thermal transport, without which the μ-ILED temperature would increase significantly (Figure 4c). The waterproof characteristics of the wireless μ-ILED system are demonstrated by results in Figure 4d and Figure S16a (SI), which show operation underwater and completely immersed in phosphate-buffered saline (PBS) solution, respectively (see Figure S16b, SI). After two weeks immersion of the system in PBS solution, no noticeable changes were observed in RF characteristics, as shown in Figure 4e.

In vivo experiments demonstrate explicitly potential applications in implantable devices. Figure 4f presents pictures of an animal model with a wireless μ-ILED system laminated conformally on a sub-dermal region and powered via inductive coupling with a primary coil at a frequency of 27.6 MHz with (left frame) and without (right frame) the skin covering in place, where the approximate depth from the skin was ~3 mm. To facilitate handling and eventual contact, this device used a silk film as a bio-resorbable, water soluble substrate. Mounting the system on the sub-dermal surface and then dissolving the silk platform with saline solution, left only the coil and μ-ILED behind, wrapped effectively on the tissue by interface water capillary interactions. A more conventional substrate, such as a sheet of PET, can also be used, as shown in Figure 4g, although with somewhat less favorable mechanics. To assess the biocompatibility of the system, we examined histological slices of tissues surrounding the implanted devices (both with and without encapsulation by a thin layer of PDMS). A representative image of histological section of tissue at the implant site, excised after 3 weeks shows absence of any severe inflammatory reaction in the neighboring tissues (Figure 4h).

These results represent the first demonstrations of wireless powering in flexible and stretchable optoelectronic devices, thereby providing some clear implications for expanded modes of use, particularly in bio-integrated applications. The RF characteristics of integrated systems show finite, but manageable, dependence on bending and stretchable deformations, and acceptable thermal behaviors, all suggesting a potential for use in implants. The same procedures and strategies should also be applicable to other classes of devices that are more complex than those illustrated here.

Experimental Section

Fabrication of InGaN μ-ILEDs: The active material stacks were grown on double polished sapphire substrates (2 inch diameter, Cermet Inc.). The composition included undoped GaN (3.8 μm), a buffer layer, n-type doped GaN (2 μm), multiple quantum wells (0.14 μm), and p-type doped GaN (0.2 μm). After rinsing with diluted HCl (HCl:DI = 1:3) for 5 min to remove the native oxide of GaN and metal ions, bi-layers of Ni (15 nm)/ Au (15 nm) for current spreading were formed on p-type GaN by sputter deposition and subsequent photolithography. Annealing in an oxygen and nitrogen atmosphere at a temperature of 500 °C for 5 min helped to reduce the contact resistances. Next, n-GaN recess regions were formed by chlorine based inductively coupled plasma reactive ion etching (ICP-RIE) through a masking layer of photoresist (AZ nLOF 2070, MicroChem.). Formation of rectangular metal contact pads (Cr (15 nm)/ Au (300 nm) on the n and p-type GaN (25×25 μm^2) using electron beam evaporation (Temescal, FC-1800) and photolithography completed the fabrication of arrays of fully formed devices on sapphire. Bonding this substrate to a silicon wafer using an indium (In) and palladium (Pd) chemical alloy prepared the stack for backside exposure with a KrF laser (Intensity = 0.9 J/cm^2, JPSA Inc.). This process enabled transfer of the devices to the silicon, bonded with an In-Pd alloy that forms between some fraction of the In and most of the Pd. Selectively etching of unalloyed In with HCl also removed residual Ga from the laser transfer, to leave isolated structures of In-Pd that hold the devices on the underlying wafer. All of the μ-ILEDs were transferred to a slab of PDMS with embossed features (3 μm in diameter, 1.2 μm in height, and 5 μm in space) on its surface; these structures provide sufficient adhesion for this transfer, but at a sufficiently weak level to allow efficient retrieval with a stamp (relief features with heights and lateral dimensions of 100 μm) designed for transfer printing. Removing the Pd (for unalloyed Pd) and Cr (adhesion layer) with commercial etchants (Transene) eliminated all of remaining the metal (besides that use for the contacts).

Animal Model Evaluations: All procedures were carried out under approved animal protocols. A female Balb/c mouse was anaesthetized with an intraperitoneal injection of a mix of ketamine–xylazine. The depth of anesthesia was monitored by palpebral and withdrawal reflexes to confirm that the animal had reached 'stage 3' of anesthesia. Once the animal was lightly anaesthetized, the back was shaved and cleaned at the incision site with 70% ethanol, followed by a betadine surgical scrub. Once stage 3 was confirmed, a small longitudinal incision was made through the skin and the sterile implants (ethylene oxide sterilized) were inserted. The incision was closed with a Dexon 5-0 suture. The animal was monitored until ambulatory and given a dose of analgesia (Buprenorphine subcutaneously) as soon as surgery was completed. The skin tissue for histology study was harvested after 3 weeks of implantation and washed in PBS, and fixed in 10% neutral buffered formalin before histological analyses. Samples were dehydrated through a series of graded alcohols, embedded in paraffin and sectioned at 8μm thickness. For histological evaluation, sections were deparaffinized, rehydrated through a series of graded alcohols, and stained with hematoxylin and eosin (H&E).

RF Characterization: Measurements were conducted with a network analyzer HP 8573D to determine the return loss, S11 (number of scanning points = 801).

Supporting Information

Supporting Information is available from the Wiley Online Library or from the author.

Acknowledgements

This material is based upon work supported in part by a National Security Science and Engineering Faculty Fellowship (J.A.R.), the U.S. Army Research Laboratory and the U.S. Army Research Office under contract number W911 NF-07-1-0618 and by the DARPA-DSO. Funding from the National Science Foundation supported research on the mechanics and processing aspects (NSF Grant Nos. ECCS-0824129 and OISE-1043143). R.-H. K. would like to thank X. Huang and the semiconductor division of Samsung Electronics for invaluable discussions and doctoral fellowships, respectively.

[1] D.-H. Kim, J. Xiao, J. Song, Y. Huang, J. A. Rogers, *Adv. Mater.* **2010**, *22*, 2108.
[2] H. C. Ko, M. P. Stoykovich, J. Song, V. Malyarchuk, W. M. Choi, C.-J. Yu, J. B. Geddes, J. Xiao, S. Wang, Y. Huang, J. A. Rogers, *Nature* **2008**, *454*, 748.
[3] J. A. Rogers, T. Someya, Y. Huang, *Science* **2010**, *327*, 1603.
[4] C.-H. Lee, Y.-J. Kim, Y. J. Hong, S.-R. Jeon, S. Bae, B. H. Hong, G.-C. Yi, *Adv. Mater.* **2011**, *23*, 4614.
[5] R.-H. Kim, D.-H. Kim, J. Xiao, B. H. Kim, S.-I. Park, B. Panilaitis, R. Ghaffari, J. Yao, M. Li, Z. Liu, V. Malyarchuk, D. G. Kim, A.-P. Le, R. G. Nuzzo, D. L. Kaplan, F. G. Omenetto, Y. Huang, Z. Kang, J. A. Rogers, *Nat. Mater.* **2010**, *9*, 929.
[6] E. C. Nelson, N. L. Dias, K. P. Bassett, S. N. Dunham, V. Verma, M. Miyake, P. Wiltzius, J. A. Rogers, J. J. Coleman, X. Li, P. V. Braun, *Nat. Mater.* **2011**, *10*, 676.
[7] D.-H. Kim, N. Lu, R. Ma, Y.-S. Kim, R.-H. Kim, S. Wang, J. Wu, S. M. Won, H. Tao, A. Islam, K. J. Yu, T.-I. Kim, R. Chowdhury, M. Ying, L. Xu, M. Li, H.-J. Chung, H. Keum, M. McCormick, P. Liu, Y.-W. Zhang, F. G. Omenetto, Y. Huang, T. Coleman, J. A. Rogers, *Science* **2011**, *333*, 838.
[8] I. Jung, J. Xiao, V. Malyarchuk, C. Lub, M. Li, Z. Liu, J. Yoon, Y. Huang, J. A. Rogers, *Proc. Natl. Acad. Sci. USA* **2011**, *108*, 1788.
[9] T. Sekitani, M. Takamiya, Y. Noguchi, S. Nakano, Y. Kato, T. Sakurai, T. Someya, *Nat. Mater.* **2007**, *6*, 413.
[10] K. D. Wise, D. J. Anderson, J. F. Hetke, D. R. Kipke, K. Najafi, *P. IEEE.* **2004**, *92*, 76.
[11] E. Y. Chow, C.-L. Yang, A. Chlebowski, S. Moon, W. J. Chappell, P. P. Irazoqui, *IEEE T. Microw. Theory.* **2008**, *56*, 3200.
[12] A. V. Corazza, J. Jorge, C. Kurachi, V. S. Bagnato, *Photomed. Laser Surg.* **2007**, *25*, 102.
[13] H. L. Liang, H. T. Whelan, J. T. Eells, M. T. T. Wong-Riley, *Neuroscience* **2008**, *153*, 963.
[14] J. L. N. Bastos, R. F. Z. Lizarelli, N. A. Parizotto, *Laser Phys.* **2009**, *19*, 1925.
[15] C. S. Xu, A. W. N. Leung, L. Liu, X. S. Xia, *Laser Phys. Lett.* **2010**, *7*, 544.
[16] D. Q. Bai, C. M. N. Yow, Y. Tan, E. S. M. Chu, C. S. Xu, *Laser Phys.* **2010**, *20*, 544.
[17] B. P. Timko, T. Dvir, D. S. Kohane, *Adv. Mater.* **2010**, *22*, 4925.
[18] S. Waxman, *J. Interv. Cardiol.* **2008**, *21*, 452.
[19] C. Balas, *Meas. Sci. Technol.* **2009**, *20*, 104020.
[20] S.-I. Park, Y. Xiong, R.-H. Kim, P. Elvikis, M. Meitl, D.-H. Kim, J. Wu, J. Yoon, C.-J. Yu, Z. Liu, Y. Huang, K.-C. Hwang, P. Ferreira, X. Li, K. Choquette, J. A. Rogers, *Science.* **2009**, *325*, 977.
[21] a) H.-S. Kim, E. Brueckner, J. Song, Y. Lid, S. Kim, C. Lud, J. Sulkin, K. Choquette, Y. Huang, R. G. Nuzzo, J. A. Rogers, *Proc. Natl. Acad. Sci. USA* **2011**, *108*, 10072; b) T.-i. Kim, Y. H. Jung, J. Song, D. Kim, Y. Li, H.-S. Kim, I.-S. Song, J. J. Wierer, H. A Pao, Y. Huang, J. A. Rogers, *Small* **2012**, *8*, 1643.
[22] J.-H. Jeon, E. J. Inigo, M. T. Reiha, T.-Y. Choi, Y. Lee, S. Mohammadi, L. P. B. Katehi, in *33rd Eur. Microwave Conf.* Horizon House Publisher, London, UK **2003**, 53.
[23] D.-H. Kim, J.-H. Ahn, W.-M. Choi, H.-S. Kim, T.-H. Kim, J. Song, Y. Y. Huang, L. Zhuangjian, L. Chun, J. A. Rogers, *Science* **2008**, *320*, 507.
[24] H. Kressel, J. K. Butler, in *Semiconductor Lasers and Heterojunction LEDs*, Academic Press, New York **1977**, p. 73.
[25] A. J. pal, R. Österbacka, K.-M. Källman, H. Stubb, *Appl. Phys. Lett.* **1997**, *70*, 2022.
[26] A. N. Laskovski, M. R. Yuce, T. Dissanayake, *IEEE Sensors J.* **2011**, *11*, 1484.
[27] S. Y. Y. Leung, D. C. C. Lam, *IEEE T Electron Pa. M.* **2007**, *30*, 200.
[28] J. P. Phillips, R. M. Langford, P. A. Kyriacou, D. P. Jones, *Physiol. Meas.* **2008**, *29*, 1383.
[29] G. Gratton, M. Fabiani, *Front. Hum. Neurosci.* **2010**, *4*, 1.
[30] E. S. Boyden, F. Zhang, E. Bamberg, G. Nagel, K. Deisseroth, *Nat. Neurosci.* **2005**, *8*, 1264.

Received: May 2, 2012
Published online: June 29, 2012

